Uptake of Nitric Acid on Ice at Tropospheric Temperatures: Implications for Cirrus Clouds†

Paula K. Hudson, John E. Shilling, and Margaret A. Tolbert*

Department of Chemistry and Biochemistry and the Cooperative Institute for Research in Environmental Sciences, University of Colorado, Boulder, Colorado 80309

Owen B. Toon

Laboratory for Atmospheric and Space Physics, Program in Atmospheric and Oceanic Science, University of Colorado, Boulder, Colorado 80309

Received: February 22, 2002; In Final Form: June 27, 2002

The uptake of nitric acid by thin ice films at temperatures from 209 to 220 K was studied using a Knudsen cell flow reactor and FTIR reflection absorption spectroscopy (FTIR−RAS). Using the measured HNO_3 uptake along with the measured ice surface areas, equilibrium coverages (Θ) and initial uptake efficiencies (γ) for HNO_3 on ice were determined. A negative temperature dependence was observed for both the Θ and γ data. The initial uptake efficiencies ranged from $\gamma = 7 \times 10^{-3}$ at $T = 209$ K to $\gamma = 3 \times 10^{-3}$ at $T = 220$ K. Using $P_{HNO_3} = 8 \times 10^{-7}$ Torr, the uptake of HNO_3 saturated at around one monolayer (ML) at $T = 213$ K and decreased with increasing temperature. At temperatures below $T = 213$ K, multiple layers of HNO_3 were adsorbed using $P_{HNO_3} = 8 \times 10^{-7}$ Torr. Using $P_{HNO_3} = 1.7 \times 10^{-6}$ Torr, temperature dependent uptake was also observed, however the transition from monolayer to multilayer uptake occurred at a higher temperature than when using a lower nitric acid pressure. A multilayer Frenkel−Halsey−Hill (FHH) model was applied to our temperature dependent data and was used to facilitate comparisons with other laboratory and field studies obtained at higher and lower nitric acid partial pressures. Our coverage values at $T > 213$ K are quantitatively lower than previous laboratory results by Abbatt, however extrapolations of our model to data by Arora et al. agree within a factor of 2. We have also compared our modeled coverages to field observations by Weinheimer et al. and Meilinger et al. of HNO_3 uptake on lee-wave and cirrus clouds, respectively. Modeled coverages fit both sets of data well but lie slightly above the Meilinger et al. data.

Introduction

Nitric acid, HNO_3, is one of the most important NO_y species in the troposphere ($NO_y = NO_x + N_2O_5 + HNO_3 + ClONO_2 + PAN + ...$). By tying up NO_x ($NO_x = NO + NO_2$) into a less photochemically active form, HNO_3 can impact photochemical ozone production and the oxidative capacity of the atmosphere. Current models overestimate the ratio of HNO_3 to NO_x by factors of two to ten.[1] This implies either a missing sink of HNO_3, a missing source of NO_x species, or a missing conversion from HNO_3 to NO_x, also known as "renoxification." Many laboratory studies have investigated heterogeneous pathways to identify a process that would correct this imbalance in models. Heterogeneous reactions of HNO_3 on soot,[2,3] aerosols and cloud droplets,[1] and dust and biomass burning particles[4−6] have all been proposed as possible pathways for HNO_3 removal or renoxification of the atmosphere. Because cirrus clouds are prevalent and have large surface areas, ice is a natural surface to consider for HNO_3 uptake and redistribution in the atmosphere.[7,8]

A number of studies have previously examined the heterogeneous removal of HNO_3 on ice using a variety of techniques. Laboratory results and models thereof predict coverages of 1×10^{14} to 1×10^{15} molecules cm^{-2} over a wide range of temperatures and pressures.[9,10,8,11] There is also a limited amount of field data for HNO_3 on cirrus.[12,13] One difficulty in comparing the laboratory data to field data is the vastly different temperature and pressure conditions under which the data were obtained. Here, we determine a relationship between gas-phase HNO_3 pressure and the resulting temperature-dependent coverage on ice films.

Our study has examined the uptake of nitric acid on ice over a range of upper tropospheric temperatures ($T = 209-220$ K) using nitric acid pressures ranging from $P_{HNO3} = 7.9 \times 10^{-7}$ to 1.7×10^{-6} Torr. In this study, we find sharp increases in nitric acid coverage, to amounts greater than a monolayer, at the lowest temperatures studied. We also find an increase in HNO_3 coverage on ice with increased HNO_3 pressure. The strong temperature and pressure dependences have not been observed in previous laboratory studies.

The observation of coverages greater than a monolayer forces a revision of the monolayer model that had been applied to the previous laboratory data.[8] The multilayer Frenkel−Halsey−Hill (FHH) model has been fit to the data from this study. The model has also been applied to a previous laboratory measurement of nitric acid uptake on ice particles and agreement is found to within a factor of 2. We also extrapolate the model to determine coverage using conditions representative of field observations by Weinheimer et al. and Meilinger et al.[12,13]

Experimental Section

The experimental setup has been described in detail previously.[14] Briefly, a Knudsen cell flow reactor[15] and Fourier

† Part of the special issue "Jack Beauchamp Festschrift". Dedicated to Jack Beauchamp, with many thanks for his guidance and support over the years.

10.1021/jp020508j CCC: $22.00
Published on Web 08/24/2002

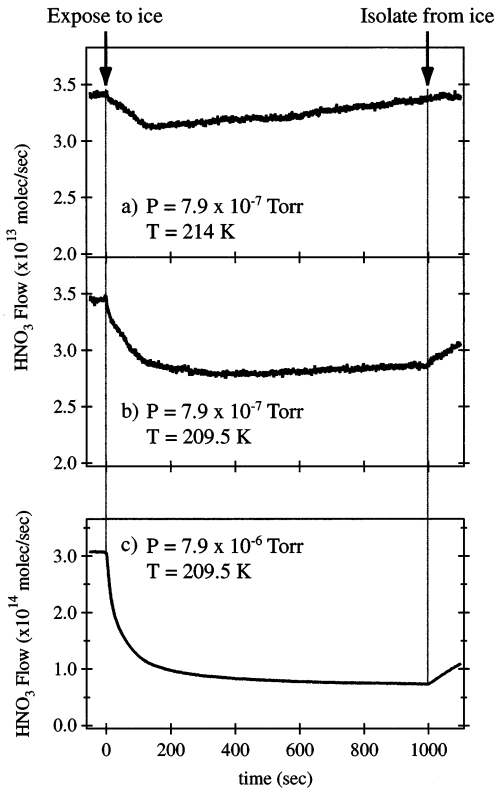

Figure 1. Mass spectrometer signal (*m*/*z* 46) calibrated to nitric acid flow versus time of exposure to ice film. The nitric acid is exposed to the ice film at $t = 0$ s and isolated from the ice film at $t = 1000$ s for the following conditions in (a) small-limited uptake, $P_{HNO_3} = 7.9 \times 10^{-7}$ Torr, $T = 214$ K, (b) large-limited uptake, $P_{HNO_3} = 7.9 \times 10^{-7}$ Torr, $T = 209.5$ K, (c) unlimited uptake, $P_{HNO_3} = 7.9 \times 10^{-6}$ Torr, $T = 209.5$ K.

transform infrared reflection absorption spectroscopy (FTIR−RAS)[16] are used to simultaneously monitor gas and condensed phases, respectively. Thin ice films are deposited on a vertically mounted, temperature controlled, gold substrate. The IR beam reflects off the gold substrate at a grazing angle of 83° from the surface normal for high sensitivity to condensed phase species. Gas-phase concentrations of HNO_3 and water are determined using the mass spectrometer, ionization gauge, and absolute capacitance manometer. A Teflon cup is positioned directly across from the gold substrate so that, when extended, it isolates the gold substrate from the rest of the chamber.

In a typical experiment, the gold substrate is first cooled to a desired temperature and a thin ice film is deposited by introducing water vapor into the chamber. The water vapor pressure is adjusted until a stable film is obtained. Film stability is determined by monitoring the OH stretching region in the FTIR−RAS. Although thermocouples are attached to the back of the gold substrate, ice film temperatures are determined using the relationship between temperature and water vapor pressure from Marti and Mauersberger.[17]

Once a stable film has been established, the Teflon cup is extended over the film, isolating it from the chamber. A flow of HNO_3 is then introduced into the chamber and monitored using the mass spectrometer to ensure a steady flow. Typical results of exposure of HNO_3 to ice films at various HNO_3 pressures and ice film temperatures are shown in Figure 1. At $t = 0$ s in Figure 1a, 1b, and 1c, the ice films are exposed to HNO_3 by retracting the Teflon cup and a drop in the HNO_3 flow is observed. It is important to note that any drop in the HNO_3 flow corresponds to HNO_3 uptake on the ice film surface because retraction of the Teflon cup results in an extremely small volume change (<0.05% of the chamber volume.) Furthermore, because the cup is made of Teflon and is never in contact with the gold substrate, no reaction takes place on the cup. If the ice surface becomes saturated with HNO_3, as in Figure 1a, the HNO_3 flow returns to its original level. If the uptake of HNO_3 does not saturate within the time scale of our experiment, as in Figure 1b or 1c, the HNO_3 flow does return to its initial value once the film is isolated.

The technique to determine the coverage of adsorbates has been discussed in detail previously.[14] Briefly, the uptake of HNO_3 onto the ice surface, as shown in Figure 1a, is equivalent to the decrease and recovery of HNO_3 flow (molecules s^{-1}) from $t = 0-1000$ s. This integrated uptake (molecules) is converted to an adsorbed HNO_3 coverage by dividing by the ice film surface area. The ice film surface area was determined using a BET measurement described in detail below.

The initial uptake efficiency, γ_{obs}, can be obtained from the initial drop in the mass spectrometer signal

$$\gamma_{obs} = \frac{A_h}{A_s}\left(\frac{F_o - F}{F}\right) \tag{1}$$

where A_h is the area of the escape orifice (0.17 cm^2), A_s is the surface area of the ice film, F_o is the initial flow of HNO_3 through the chamber, and F is the value after exposure to the film. With respect to Figure 1a, $F_o = 3.4 \times 10^{13}$ molecules s^{-1} and $F = 3.1 \times 10^{13}$ molecules s^{-1}. The uptake efficiency, γ_{obs}, has a time dependence and goes to zero at long times as the ice surface becomes saturated with HNO_3. However, HNO_3 is extremely sticky and adsorbs to the walls of the chamber. Therefore, when HNO_3 adsorbs to the ice film, HNO_3 desorbs from the chamber walls to compensate for this loss creating an additional HNO_3 source. This additional source of HNO_3 can be accounted for in the uptake efficiency according to Aguzzi and Rossi[18]

$$\gamma_{true} = \gamma_{obs} + \frac{A_h N}{A_s t_{ss} F} \tag{2}$$

where N is equal to the total number of HNO_3 molecules that desorb from the walls creating an additional source of HNO_3, and t_{ss} is the time required for the mass spectrometer signal to reach its steady-state value after the film has been exposed to the nitric acid.

Determination of Ice BET Surface Area. Typically, the surface coverage (molecules cm^{-2}) of a species on ice is obtained by dividing the number of molecules lost from the gas phase to the surface by the geometric surface area of the ice. During vapor deposition of ice films at temperatures greater than $T = 211$ K, a large amount of scatter was observed with FTIR−RAS indicating rough film surfaces. For this reason, the true surface area of the ice films is experimentally determined through BET (Brunauer, Emmett, and Teller) measurements using butane as an adsorbate.

The adsorption of butane was measured on smooth ice films, deposited at $T = 160$ K, and rough ice films, deposited at $T = 211-219$ K. After ice deposition at either the low or high temperature, the temperature of the ice film was decreased to $T = 125$ K for butane adsorption. The difference between the amount of adsorbed butane on a smooth versus rough ice film will be used to determine a true ice film surface area.

For our surface area determination we have measured the pressure dependent BET isotherm for butane on ice at $T = 125$

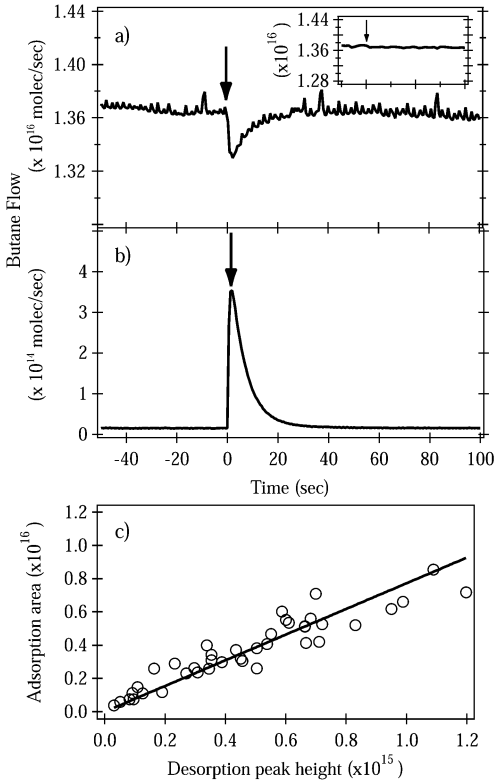

Figure 2. Mass spectrometer signal calibrated to butane flow upon (a) exposure to ice film at $T_{\text{ice film}} = 125$ K, and (b) isothermal desorption of butane from ice film into evacuated chamber at $T_{\text{ice film}} = 125$ K. The inset in (a) is butane flow (7.95×10^{16} molecules/s^{-1}) vs time ($-5-20$ s) upon exposure to blank gold substrate at $T_{\text{surface}} = 200$ K. The arrows in (a), (a) inset, and (b) indicate where the Teflon cup was retracted from the surface. c) Integrated adsorption peak area (molecules) vs desorption peak height (molecules/s^{-1}) with linear fit forced through zero.

K. It has the form

$$\frac{\Theta}{\Theta_{\max}} = \frac{c \bullet S}{(1 - S)[1 + (c - 1)S]} \tag{3}$$

where Θ is the coverage at a pressure P, $\Theta_{\max} = 2.77 \times 10^{14}$ molecules cm^{-2} (the maximum monolayer coverage), S is the saturation ratio ($S = P/P^{o}$) and P^{o} is the experimentally determined vapor pressure of butane at $T = 125$ K. The constant c is a fitting variable. $\Theta_{\max}$ is calculated from the density and molecular weight of butane. If we assume a butane molecule is a sphere with density $\rho = 0.59$ g/mL,[19] then the radius of the spherical butane can be determined and, in turn, a cross-sectional area of butane is determined. We calculate a cross-sectional area of 3.61×10^{-15} cm^2 molecule^{-1} of butane, or a maximum monolayer coverage of $\Theta_{\max} = 2.77 \times 10^{14}$ molecules cm^{-2}.

The adsorption of butane on ice is performed using the same technique as for HNO_3 adsorption. Figure 2a shows the uptake of butane on a smooth ice film deposited at $T = 160$ K then cooled to $T = 125$ K for butane exposure. For comparison, the inset in Figure 2a shows butane exposure to a blank gold substrate at $T = 200$ K using the same initial butane flow. No decrease in the signal is observed, demonstrating that the decrease in butane signal is due to adsorption onto the ice film and not due to the small volume expansion when the Teflon cup is retracted. At $T = 125$ K, background levels of H_2O in the chamber would deposit onto the gold substrate. Therefore at $T = 125$ K, a true "blank" experiment where no ice is deposited onto the substrate cannot be performed.

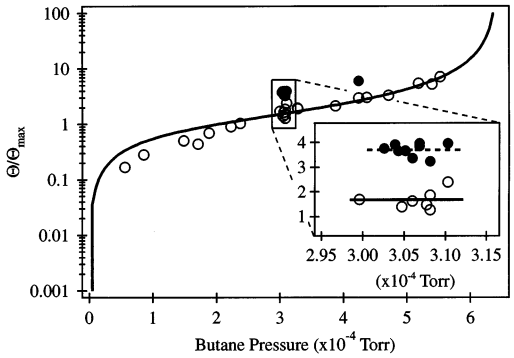

Figure 3. Butane coverage normalized by dividing by the coverage of one monolayer as a function of butane exposure pressure for smooth films deposited at $T = 160$ K (open circles), and films deposited at $T = 211-219$ K (solid circles). The open circles are fit with a BET model. The boxed area is enlarged, shown as inset, and averages through the data have been added as solid line for the open circles and a dashed line for the solid circles.

Figure 2b shows the isothermal desorption of butane from the ice film at $T = 125$ K. After butane adsorption, the ice surface is again isolated from the butane flow and the chamber is evacuated. Once the chamber has reached its base pressure, the Teflon cup is retracted from the surface (indicated by arrow) and any butane that is physisorbed to the ice isothermally desorbs.

As was described previously, the integrated area of the adsorption curve can be used to obtain the number of molecules lost to the surface. However, due to the high pressures of butane used in these experiments, $P = 5 \times 10^{-5} - 4 \times 10^{-4}$ Torr, the adsorption curves were fairly noisy and often difficult to integrate. For this reason, the peak height of the isothermal desorption peak was used analogously to that of the adsorption area. As shown in Figure 2c, there is a linear relationship between the area of the adsorption curve and the peak height of the desorption peak. Thus, the desorption peak height is converted to an integrated adsorption area using the slope in Figure 2c (7.73 molecules (peak height)$^{-1}$). A plot of $\Theta/\Theta_{\max}$ versus pressure of butane is shown in Figure 3 as open circles. A fit to these data using the BET model (Equation 3) with $c = 4.6$ is shown as the solid line. The BET model offers a reasonable approximation to the butane data adsorbed to smooth ice films.

The coverage of butane on rough ice films deposited from $T = 211-219$ K and then decreased to $T = 125$ K for butane exposure is shown as solid circles in Figure 3. As in the case of the smooth ice film coverage calculation, the ice surface area is assumed to be the geometric area of the gold substrate, 5.07 cm^2. As shown in the inset in Figure 3, this coverage is approximately 2.27 times larger than the coverage on a smooth film. Therefore, the surface area of the rough ice film must be 2.27 times larger than the substrate area, represented by the smooth film, yielding an ice film surface area of 11.5 cm^2 for the rough ice film vapor deposited at $T = 211-219$ K. No variation in surface area within this temperature range is observed.

Results and Discussion

Regimes of Nitric Acid Uptake. Figure 1 shows three different types of uptake observed upon exposure of nitric acid to ice films under varying conditions of nitric acid pressure and ice film temperature. The magnitude of the drop in flow varies with ice film temperature as well as nitric acid pressure. Note that the nitric acid flow in parts a and b are on the same scale

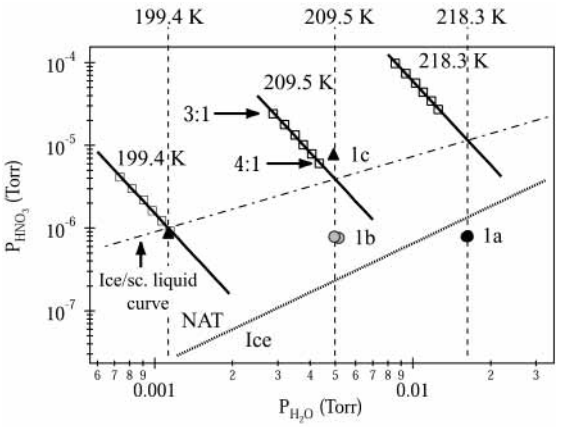

Figure 4. HNO_3 and H_2O phase diagram with vapor pressures of HNO_3/H_2O supercooled solutions at three temperatures, $T = 199.4$, 209.5, and 218 K from Hanson data 1990. The dot−dashed line is the ice/supercooled HNO_3/H_2O solution equilibrium curve. For pressures above this line, a supercooled solution can form. The small-limited uptake (black circles at $P_{H_2O} = 0.016$ Torr, $T = 218$ K) and large-limited uptake (gray circles at $P_{H_2O} = 0.005$ Torr, $T = 209.5$ K) are well below the relative supercooled solution lines. However, the unlimited uptake (solid triangles) at $P_{H_2O} = 0.005$ Torr ($T = 209.5$ K) and $P_{H_2O} = 0.001$ Torr ($T = 199.4$ K) are above or on the supercooled solution lines. The gray line represents the ice/NAT line from Hanson and Mauersberger, GRL, 1988.

and that the nitric acid flow in part c is on an order of magnitude larger scale.

In Figure 1a ($P_{HNO_3} = 7.9 \times 10^{-7}$ Torr, $T = 214$ K) a small decrease in the nitric acid flow is observed after exposure to the ice film followed by a gradual recovery to its original level. As stated previously, this indicates an equilibrium coverage of HNO_3 on ice has been attained. A slightly larger drop is observed in the HNO_3 flow in Figure 1b ($P_{HNO_3} = 7.9 \times 10^{-7}$ Torr, $T = 209.5$ K) followed by a gradual increase in the flow rate. Although not observed on this time scale, with longer exposures the HNO_3 flow continues to return to its original value. For future reference, Figures 1a and 1b will be referred to as small- and large-limited uptake, respectively. When the ice film temperature is kept constant at $T = 209.5$ K, and the initial HNO_3 pressure is increased an order of magnitude, as shown in Figure 1c, ($P_{HNO_3} = 7.9 \times 10^{-6}$ Torr, $T = 209.5$ K), an even larger drop in signal is observed followed by a continually decreasing signal. This type of uptake is also observed when $P = 7.9 \times 10^{-7}$ Torr and $T = 199.4$ K. This type of uptake will be referred to as unlimited uptake and will later be identified as being due to formation of a supercooled HNO_3/H_2O solution.

Previous studies of HNO_3 on ice have observed uptake behavior that depends on the phase of HNO_3/H_2O formed as a result of the interaction. Zondlo et al. observed enhanced nitric acid uptake on thin ice films with the formation of a supercooled HNO_3/H_2O solution relative to uptake on ice.[9] An HNO_3/H_2O phase diagram supported these data being taken in the supercooled solution regime. To help explain the three types of uptake observed here, we too have examined these regimes with respect to the HNO_3/H_2O phase diagram shown in Figure 4. The open squares are supercooled HNO_3/H_2O solution vapor pressures as determined by Hanson[20] with solid lines fit to the data. The gray line is the ice/NAT equilibrium line determined by Hanson and Mauersberger.[21] The dot−dashed line is the ice/supercooled HNO_3/H_2O solution equilibrium curve. The points 1a, 1b, and 1c in Figure 4 correspond to the initial conditions of the experiments and not to equilibrium conditions. Points 1a and

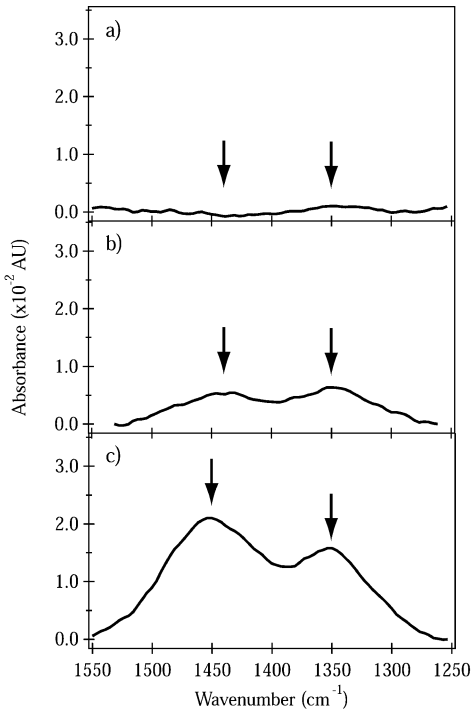

Figure 5. FTIR−RAS spectra of the asymmetric NO_3^- stretches for (a) small-limited uptake, $P_{HNO_3} = 7.9 \times 10^{-7}$ Torr, $T_{ice\ film} = 214$ K, (b) large-limited uptake, $P_{HNO_3} = 7.9 \times 10^{-7}$ Torr, $T_{ice\ film} = 209.5$ K, (c) unlimited uptake, $P_{HNO_3} = 7.9 \times 10^{-6}$ Torr, $T_{ice\ film} = 209.5$ K.

1b in Figure 4, corresponding to small- and large-limited uptake experiments respectively, are well below their corresponding supercooled HNO_3/H_2O solution isotherms as well as below the ice/supercooled HNO_3/H_2O solution equilibrium curve. Therefore, under these experimental conditions, it is thermodynamically impossible to form supercooled solutions. Point 1c in Figure 4, corresponding to an unlimited uptake experiment, is above and to the right of its corresponding supercooled HNO_3/H_2O solution isotherm. Therefore, under these experimental conditions, it is thermodynamically possible to form a supercooled solution. Another data point exists on the $T = 199.4$ K supercooled HNO_3/H_2O solution isotherm. This point also can form a supercooled solution. Both points 1b and 1c are above the ice/NAT equilibrium line and, therefore, in a regime where NAT is the most thermodynamically stable form. However, our IR spectroscopic probe shows that NAT does not form in any of the experiments here, as discussed further below.

Figure 5 shows the IR spectrum in the region of the asymmetric NO_3^- peaks (1500−1250 cm^{-1}) for the three HNO_3 uptake regimes shown in Figure 1. For all three spectra in Figure 5, a baseline has been subtracted for easier interpretation. No NO_3^- peaks are present in Figure 5a as expected due to the small submonolayer coverage ($\Theta = 4 \times 10^{14}$ molecules cm^{-2}). The coverage of HNO_3 is equivalent in Figure 5b and 5c, $\Theta = 1.3 \times 10^{15}$ molecules cm^{-2}. It can be seen that for the large-limited uptake in Figure 5b, the lower wavenumber peak at 1340 cm^{-1} is larger than the higher wavenumber peak at 1440 cm^{-1}. The reverse is true for the supercooled HNO_3/H_2O solution in Figure 5c.

We have compared our supercooled HNO_3/H_2O solution spectrum (Figure 5c) with that of Zondlo et al.[22] Dividing the lower wavenumber peak amplitude (1.5×10^{-2}) by the higher wavenumber peak amplitude (2×10^{-2}) yields a value of 0.75. This is in close agreement with the ratio of 0.76 from Zondlo et al. for a supercooled 4:1 H_2O:HNO_3 solution,[22] which is expected from the phase diagram in Figure 4. Zondlo et al.

verifies his spectra by comparison to spectra derived from optical constants from Toon et al.[22,23]

Although we do not believe Figure 5b to be representative of a supercooled solution, we can again compare the spectrum to a previously determined supercooled HNO_3/H_2O solution spectrum from that of Zondlo et al.[22] If we divide the lower wavenumber peak amplitude (0.6×10^{-2}) by the higher wavenumber peak amplitude (0.5×10^{-2}) in Figure 5b, then we obtain a ratio of 1.2. This value is in close agreement with the ratio of 1.13 from Zondlo et al. for a supercooled 2:1 H_2O:HNO_3 solution.[22] Referring to the phase diagram in Figure 4, at $T = 209.5$ K, the nitric acid pressure required to form a supercooled 2:1 H_2O:HNO_3 solution would be greater than 3×10^{-5} Torr HNO_3. Because the nitric acid pressure used in this experiment is $P_{HNO3} = 7.9 \times 10^{-7}$ Torr, we can say that the spectrum in Figure 5b does not correspond to a supercooled HNO_3/H_2O solution.

It should be noted that neither spectrum from Figure 5b or 5c resembles that of NAT. Although both experiments have initial HNO_3 pressure and ice film temperature conditions within the NAT stability regime (see points 1b and 1c in Figure 4), NAT is not observed.

Initial Uptake Efficiencies for HNO_3 on Ice. Because we have now determined that the small- and large-limited uptakes are not supercooled solutions and the unlimited uptake is a supercooled solution, we will discuss these results separately. The initial uptake efficiency of HNO_3 on ice can be calculated from the magnitude of the initial drop in signal (from Figure 1a and 1b) and eq 2. The value N/t_{ss} required for eq 2 was obtained using data for $P_{HNO_3} = 7.9 \times 10^{-7}$ Torr and $T = 208-211$ K. This value is determined by integrating the number of molecules of HNO_3 that re-adsorb to the walls (N) after the Teflon cup is closed and dividing by the time it takes for the initial drop in HNO_3 signal to reach a minimum (t_{ss}). For our purposes, t_{ss} is represented by the time it takes for the flow to decrease by 90% of the full difference. For small- and large-limited uptake experiments, a value of $N/t_{ss} = 4.8 \times 10^{12} \pm 1.4 \times 10^{12}$ molecules s^{-1} is applied. A value of $N/t_{ss} = 6.4 \times 10^{13} \pm 1.3 \times 10^{13}$ molecules s^{-1} was applied to the supercooled solution data.

As was shown earlier, we have two experiments that correspond to formation of a supercooled HNO_3/H_2O solution as determined by both the phase diagram (the solid triangles in Figure 4) and spectroscopic evidence (Figure 5c). Our data, shown as open squares in Figure 6, show a slight temperature dependence with $\gamma_{true} = 0.11$ at $T = 199.4$ K and $\gamma_{true} = 0.06$ at $T = 209.5$ K. A recent study by Aguzzi and Rossi, which accounts for the wall reactions of HNO_3, reports uptake efficiencies for HNO_3 on ice from $T = 180-211$ K with values shown as asterisks in Figure 6.[18] The pressures used in the Aguzzi and Rossi experiments range from $P_{HNO3} = 2 \times 10^{-8} - 2 \times 10^{-5}$ Torr. Aguzzi and Rossi report temperature-dependent uptake efficiencies for a number of experiments used for phase composition studies in which all HNO_3 pressures are within the supercooled HNO_3/H_2O solution formation regime.[24] There is good agreement between these data and our temperature-dependent uptake efficiencies in the supercooled HNO_3/H_2O solution regimes. However, Aguzzi and Rossi find that while the uptake efficiency depends on temperature, the uptake efficiency is independent of HNO_3 pressure. This differs from our observation of a large HNO_3 pressure dependence, seen at $T = 210$ K, with much larger uptake efficiencies with the formation of a supercooled solution.

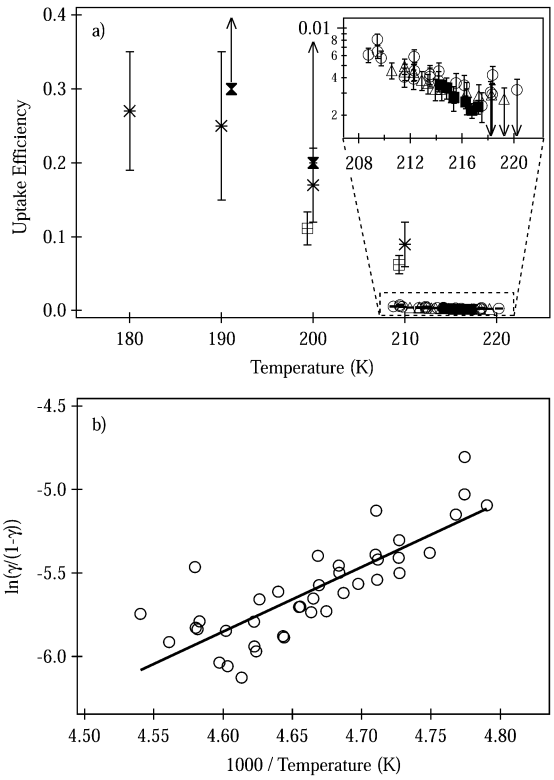

Figure 6. (a) Initial uptake efficiency as a function of ice film temperature for $P_{HNO_3} = 7.9 \times 10^{-7}$ (open circles), 8.5×10^{-7} (open triangles), and 1.7×10^{-6} (filled squares) Torr. Hanson (filled hourglass) and Aguzzi and Rossi (asterisks) data are included for comparison. Two points from the formation of the supercooled HNO_3/H_2O solution using $P_{HNO_3} = 7.9 \times 10^{-7}$ and 7.9×10^{-6} Torr are shown as open squares. (b) Plot to determine ΔH and ΔS of HNO_3 on ice using the initial uptake efficiency. The symbols are initial uptake efficiency data for the above three pressures. The line is the least-squares fit to the data.

Within our data set of the small- and large-limited uptake, there is a close agreement of initial uptake efficiencies among all three HNO_3 pressures, $P_{HNO_3} = 7.9 \times 10^{-7}$, 8.5×10^{-7}, and 1.7×10^{-6} Torr as shown by the inset in Figure 6. A negative temperature dependence exists with values ranging from $\gamma_{true} = 7 \times 10^{-3}$ at $T = 209.5$ K decreasing to $\gamma_{true} = 3 \times 10^{-3}$ at $T = 220$ K. Although the data points at $T > 217$ K appear to level out, these points are extremely difficult to measure and should be used as upper limits. Atmospheric implications of the uptake efficiencies on ice within the small- and large-limited uptake regime will be addressed later.

Other previous studies have also reported uptake efficiencies of HNO_3 on ice. Hanson reported values from flow-tube studies of HNO_3 uptake on ice of $\gamma \geq 0.3$ at $T = 191$ K and $\gamma \geq 0.2$ at $T = 200$ K[25] shown as the filled hourglasses in Figure 7. The P_{HNO_3} in Hanson's experiments were 8×10^{-8} Torr and 3×10^{-7} Torr at $T = 191$ K and $T = 200$ K, respectively. Under these nitric acid pressure and ice film temperature conditions, a supercooled HNO_3/H_2O solution should not form, but NAT formation is thermodynamically possible. However, these results do not have spectroscopic evidence of the film composition. Regardless, because our small- and large-limited uptake data does not extend to temperatures as low as Hanson reported and without full knowledge of the composition of the films, we cannot make any direct comparison with Hanson's results. We can say that our small- and large-limited uptake data should not be extrapolated beyond the temperature range of this study.

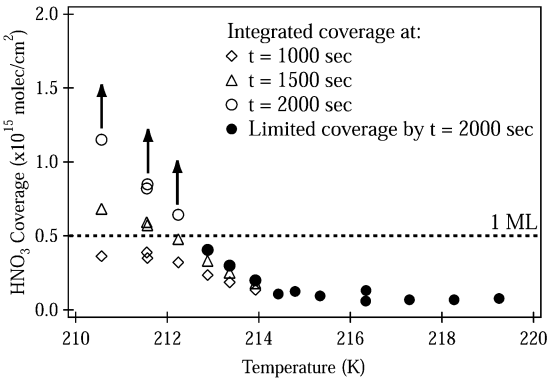

Figure 7. Nitric acid coverage as a function of ice film temperature and exposure time. The open symbols represent coverages that have not yet saturated. The arrows indicate that the coverages are still increasing. The solid symbols represent coverages that are saturated by $t = 2000$ s.

Abbatt reported an uptake efficiency of HNO_3 greater than 0.2 in his flow-tube studies of HNO_3 uptake on ice films.[10] Although his studies covered a wider range of temperatures relative to this study, this value is taken from an experiment performed at $T = 218$ K which falls within the temperature range used in the present work. The pressures used in the Abbatt study and ours are comparable. The Abbatt uptake efficiency is much larger than our reported values for small- and large-limited uptake. This value is also larger than the expected value based on the decreasing γ for the supercooled solutions as temperature increases from our work and Aguzzi and Rossi. The reasons for the differences between our values and Abbatt are not clear. One possibility for this difference is discussed in greater detail when comparing the HNO_3 coverage from the Abbatt study to that presented here.

Zondlo et al. report a lower limit of an HNO_3 uptake efficiency of $\gamma \geq 0.005$.[9] This value is taken from an experiment performed at $T = 211$ K and at a similar nitric acid pressure to the present conditions. Spectroscopic evidence was available in this study and formation of a supercooled HNO_3/H_2O solution was not observed in this case. Even though the study by Zondlo et al. was performed in the same chamber as this study, major chamber revisions have taken place. For example, in the Zondlo et al. study, a butterfly valve separated two chambers. When the ice film was exposed to the HNO_3, a relatively clean chamber is also exposed, accounting for a large amount of wall loss. However, the same type of additional source of HNO_3 from the walls of the lower chamber also exists. Without being able to account for the complex adsorption and desorption processes we are left with this result being fortuitously in line with current results.

Modeling the Uptake Efficiency. The uptake efficiency in the limited uptake regime can be modeled following the approach of Boudart and Djéga−Mariadassou for gas uptake onto solids.[26] The uptake on ice can be viewed as a two step process with gaseous HNO_3 (A_g) first physisorbing to the surface (A_p) followed by chemisorption (A_c)

$$A_g \underset{k_d}{\overset{\alpha k_{coll}}{\rightleftharpoons}} A_p \xrightarrow{k_a} A_c \tag{4}$$

Physisorption can be viewed as molecular HNO_3 weakly interacting with the ice, whereas chemisorption may involve HNO_3 ionization and incorporation into the ice lattice with hydrogen bonding. The rate constants for physisorption, desorption, and chemisorption are αk_{coll}, k_d, and k_a, respectively, where α is the mass accommodation coefficient which we are assuming is unity. The initial uptake efficiency, γ is equal to

$$\gamma = \frac{\text{adsorption rate}}{\text{collision rate}} = \frac{k_a A_p}{k_{coll} A_g} \tag{5}$$

Using eq 4 and assuming a steady-state approximation for A_p results in

$$A_p = \frac{\alpha k_{coll} A_g}{k_d + k_a} \tag{6}$$

Combining eqs 5 and 6 and using $\alpha = 1$, a relationship between the initial uptake efficiency and k_a and k_d is established

$$\gamma = \frac{1}{1 + k_d/k_a} \tag{7}$$

Following Jayne et al.,[27] the expression for the ratio of rate constants can be rewritten in terms of the observed Gibbs free energy barrier of the transition state to chemisorbed HNO_3 relative to the gas phase

$$\frac{k_a}{k_d} = \exp\left(\frac{-\Delta G_{obs}^{\ddagger}}{RT}\right) \tag{8}$$

Combining eqs 7 and 8 and substituting $\Delta G_{obs}^{\ddagger} = \Delta H_{obs} - T\Delta S_{obs}$ yields

$$\ln\left(\frac{\gamma}{1 - \gamma}\right) = \frac{-\Delta G_{obs}^{\ddagger}}{RT} = \frac{-\Delta H_{obs}}{RT} + \frac{\Delta S_{obs}}{R} \tag{9}$$

Therefore, from a plot of the left side of eq 9 versus inverse temperature (shown in Figure 6b), the ΔH_{obs} and ΔS_{obs} can be determined. From Figure 6b and Equation 9 we determine $\Delta H_{obs} = -7.6$ kcal/mol and $\Delta S_{obs} = -47$ cal/mol K. Jayne et al. measured the uptake of HNO_3 by water surfaces and determined $\Delta H_{obs} = -6.6$ kcal/mol and $\Delta S_{obs} = -27.6$ cal/mol K.[27] Although it was not an anticipated result, our value for ΔH_{obs} is quite comparable to that found by Jayne et al. In contrast, our ΔS_{obs} is a much larger negative number. Perhaps the incorporation of the dissociated HNO_3 into the ice lattice could account for the observed differences in ΔS_{obs} for ice versus water.

Using the thermodynamic values obtained, the initial uptake efficiency of HNO_3 on ice can be fit to the following equation (obtained by rearranging eq 9)

$$\gamma = \frac{\exp(-\Delta G_{obs}^{\ddagger}/RT)}{1 + \exp(-\Delta G_{obs}^{\ddagger}/RT)} \tag{10}$$

where $\Delta G_{obs}^{\ddagger} = \Delta H_{obs} - T\Delta S_{obs}$. This equation represents our HNO_3 uptake data on ice well from $T = 209$ to 220 K using $\Delta H_{obs} = -7.6$ kcal/mol and $\Delta S_{obs} = -47$ cal/mol K.

Equilibrium Coverages of HNO_3 on Ice. Figure 7 summarizes the equilibrium coverage of nitric acid on ice at $P_{HNO_3} = 8.5 \times 10^{-7}$ Torr, in both the small- and large-limited uptake regimes. For the small-limited uptake experiments, solid circles, the equilibrium coverage has been calculated directly from the integrated uptake. However, in the cases of the large-limited uptake, the signal does not fully return to its original flow within the time scale of our experiments (Figure 1b). For these cases, integrated coverages depend on the length of exposure (i.e., the longer exposure yields a greater coverage.) The time-dependent coverages are shown in Figure 7 as open symbols as a function

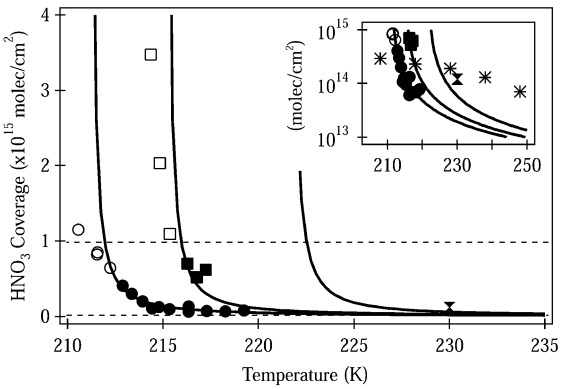

Figure 8. Nitric acid coverage as a function of ice film temperature at three different pressures, $P = 8.5 \times 10^{-7}$ Torr (solid circles), $P = 1.7 \times 10^{-6}$ Torr (solid squares) from this study, and $P = 5.0 \times 10^{-6}$ Torr (solid hourglass) from Arora et al. 1999. The open symbols represent coverages that have not yet saturated. The solid symbols represent coverages that are saturated either by or before $t = 2000$ s. The curve through all three data sets is from the FHH model that was fit to the lowest pressure data. The pressure was adjusted for the two higher pressure curves. The boxed region is duplicated in the inset on a semilog plot with added Abbatt data 1997.

of time. The arrows over the four experiments in Figure 7 are to denote that the coverage is still increasing after $t = 2000$ s of nitric acid exposure to the ice film. It can be seen that approximate monolayer HNO_3 coverages ($\Theta_{max} \approx 5 \times 10^{14}$ molecules cm^{-2} calculated by techniques described for butane) form around $T = 213$ K and decreases as temperature increases. At temperatures less than $T = 213$ K, coverages greater than one monolayer form for $P_{HNO_3} = 8.5 \times 10^{-7}$ Torr.

Figure 8 shows HNO_3 coverage data at $t = 2000$ s as a function of ice film temperature at two pressures $P_{HNO_3} = 8.5 \times 10^{-7}$ Torr (open and solid circles) and $P_{HNO_3} = 1.7 \times 10^{-6}$ Torr (open and solid squares) from this study where the open symbols again represent large-limited uptake experiments (Figure 1b). The $P_{HNO_3} = 7.9 \times 10^{-7}$ Torr data is not shown for clarity because the coverage values are very close to the $P_{HNO_3} = 8.5 \times 10^{-7}$ Torr data. For comparison, the data point from a study of HNO_3 uptake on ice particles by Arora et al. at $P_{HNO_3} = 5.0 \times 10^{-6}$ Torr (solid hourglass) has been included.[11]

Modeling the Equilibrium Coverage. The solid lines in Figure 8 represent a multilayer Frenkel−Halsey−Hill (FHH) model that has been applied to the data. The form of the FHH model is

$$\left(\frac{\Theta}{\Theta_{max}}\right) = \left\{\frac{A}{\ln\left(\frac{P^o}{P}\right)}\right\}^B \qquad (11)$$

where P^o was chosen to be the vapor pressure of a 35 wt % HNO_3/H_2O solution (6.5:1 H_2O:HNO_3 solution) determined by interpolating data provided by JaeckerVoirol et al.[28]

$$\log_{10} P^o(\text{Torr}) = \left(\frac{-3431.4}{T(\text{K})}\right) + 10.184 \qquad (12)$$

and P is the pressure of nitric acid used in the experiment. The vapor pressure of a 35 wt % HNO_3/H_2O solution was used because it provided the best fit to the data. The maximum coverage of HNO_3 for one monolayer, Θ_{max}, has been set to be 5×10^{14} molecules cm^{-2}. The constants A and B have been determined by a best fit to the $P_{HNO_3} = 8.5 \times 10^{-7}$ Torr data and are $A = 0.25$ and $B = 1.3$. The model was only fit to the $P_{HNO_3} = 8.5 \times 10^{-7}$ Torr data. The curves through the $P_{HNO_3} = 1.7 \times 10^{-6}$ Torr data and the Arora et al. data, $P_{HNO_3} = 5 \times 10^{-6}$ Torr, were created by changing only the pressure term, P, in eq 11. The curve is not expected to fit the open symbols for either pressure as these are, as in Figure 7, coverages that are still increasing as a function of exposure time. Because we do not have data to fit the lowest temperature data, the model should only be used over the temperature range for which data exist. The inset in Figure 8 shows the coverage data on a log scale with an extended temperature scale. For comparison, data from Abbatt (asterisks) from $T = 208-248$ K have been added for $P_{HNO_3} = (6-9) \times 10^{-7}$ Torr. The agreement between our FHH model and the Arora et al. data on ice particles using the FHH model is within a factor of 2. This agrees well with the overall uncertainty they state in their results.[11] The agreement with the data of Abbatt is less favorable. Possible reasons for the discrepancy are discussed further below.

Comparison of HNO_3 Coverage to Previous Results. A significant difference exists between the present results and those of Abbatt.[10] Abbatt observes pressure independent uptake of HNO_3 on ice of $\Theta = 2 \times 10^{14}$ molecules cm^{-2} for HNO_3 pressures ranging from 1×10^{-7} Torr to 3×10^{-6} Torr at $T = 228$ K. He also reports a slight negative temperature dependence from $T = 208$ K to 248 K of $\Theta = 3 \times 10^{14}$ molecules cm^{-2} to 1×10^{14} molecules cm^{-2} for $P_{HNO_3} = 6 \times 10^{-7}$ Torr to 9×10^{-7} Torr. Abbatt determines his coverages by integrating the HNO_3 signal until it recovers to two-thirds its original value. These could essentially be considered large-limited uptake experiments with reported lower limits to the coverage.

The Abbatt data differs from the present study in that he observes pressure independent uptake and that his values for coverage generally are greater than those reported here for a similar HNO_3 pressure range. This is with the exception of a point at $T = 208$ K which is below the value predicted by our model. Again, Abbatt's points can be considered lower limits due to his integration technique.

While Abbatt's ice surface area is not quantified, he does report that his films are relatively smooth although not measured on a molecular level. In our work, we observe a factor of 2 difference in surface area for ice at temperatures below and above $T = 200$ K. If Abbatt has underestimated his ice surface area, his reported coverage would decrease bringing his data toward our data. Another attempt to reconcile our data with Abbatt's is to look at differences in ice film stability. Spectroscopically, we have established our ice film stability throughout HNO_3 exposures. Abbatt reports that nearly all experiments were performed at the ice frost point and that water was added to maintain the ice film. In personal communications, Abbatt has stated that he believes his films are either stable, at 100% relative humidity, or slightly desorbing, less than 100% relative humidity. However, it is not possible for him to know the exact relative humidity to within 2%. We have calculated that if the pressure over the film were 2% higher than the vapor pressure, corresponding to a temperature error of only 0.15 to 0.2 K, the film would be growing at a rate of 0.05−1.5 μm s^{-1} when the temperature of the film ranges from $T = 218-248$ K, respectively. Thus, a 92−2600 μm film could be deposited in the $t = 1720$ s time scale of his experiments. The solubility data from Thibert and Dominé show that the above-mentioned film thicknesses could contain from $\Theta = 1.4 \times 10^{14} - 5.5 \times 10^{14}$ molecules cm^{-2} HNO_3, respectively.[29] If indeed the HNO_3 was in the ice and not just adsorbed to the surface, one would predict a temperature dependence just like that observed by Abbatt. If this explanation is correct, then it implies that during film

TABLE 1: Data Collected from Weinheimer et al. and Meilinger et al. for Figure 9

ref	T (K)	P (mbar)	gas-phase HNO_3 (pptv)	calculated gas-phase HNO_3 ($\times 10^{-8}$ Torr)	condensed NO_y (pptv)	surface area (μm^2 cm^{-3})	calculated NO_y coverage ($\times 10^{13}$ molec cm^{-2})
Weinheimer et al.	209[a]	193[b]	25−75[c]	0.36−1.09	25−75[c]	2000[c]	0.84−2.51
Meilinger et al.	196[d]	200[e]	25−110[d,f]	0.38−1.65	2−8[d,f]	419[d]	0.35−1.40

[a] Jensen et al.[31] [b] Baumgardner et al.[32] [c] Weinheimer et al.[12] [d] Meilinger et al.[13] [e] Schiller et al.[33] [f] Feigl et al.[34]

growth, ice may take up HNO_3 to the solubility limit. At ice film equilibrium, however, surface effects dominate the HNO_3 uptake.

Arora et al. performed uptake experiments of HNO_3 on 0.5 μm diameter ice particles. A saturated coverage of $\Theta = 1.2 \times 10^{14}$ molecules cm^{-2} at $P_{HNO_3} = 5 \times 10^{-6}$ Torr and $T = 230$ K was determined. The Arora et al. results are within a factor of 2 of our extrapolated model. This is within the error reported in their paper. Furthermore, the surface area of the ice particles in Aurora et al. has been well characterized using spectroscopic techniques. In contrast to the data of Abbatt on ice films, solubility of HNO_3 in the ice particle is not an issue due to the small size of the particles. Calculations show that the maximum HNO_3 effective coverage obtainable due to solubility into the small particles is three decades below what is reported. Therefore, we believe the Arora et al. data reports uptake of HNO_3 on the ice surface and is not influenced by bulk uptake. This result is in good agreement with our extrapolated model which reports uptake of nitric acid on an ice film. Additional temperature and pressure dependent experiments of HNO_3 uptake on ice particles would greatly help in investigating the differences between the present data and the studies by Abbatt.

Atmospheric Implications. The initial uptake efficiency data can be used to determine the lifetime of gaseous HNO_3 with respect to heterogeneous loss on cirrus cloud particles within the kinetic limit, assuming the particles are in equilibrium and not growing or evaporating. The heterogeneous reaction rate k_{het} is related to the initial uptake efficiency as

$$k_{het} = \frac{\gamma < \upsilon > A}{4} \tag{13}$$

where $\langle \upsilon \rangle$ is the average molecular velocity and A is the surface area density of the heterogeneous surface. The gas-phase lifetime of the species, τ, is defined as $1/k_{het}$.

For the uptake efficiency data reported here, a range of lifetimes at the kinetic limit can be determined using the range in uptake efficiencies, $\gamma = 7 \times 10^{-3}$ at $T = 209$ K decreasing to $\gamma = 3 \times 10^{-3}$ at $T = 220$ K, and the range in possible cirrus cloud surface areas, A = 20−20 000 μm^2 cm^{-3}. Using the range of initial uptake efficiencies, the lifetime, τ, of nitric acid with respect to heterogeneous loss to a 20 μm^2 cm^{-3} cloud would be $\tau = 25$ to 59 h for $\gamma = 7 \times 10^{-3}$ to 3×10^{-3}, respectively. Many cirrus clouds will not exist for as long as 24 h, and therefore, it is unlikely that the HNO_3 in the gas phase will be significantly depleted. However, this time drops as the size of cloud increases to 20 000 μm^2 cm^{-3}. In this case the lifetime with respect to heterogeneous loss ranges from $\tau = 1.5$ to 3.5 min for $\gamma = 7 \times 10^{-3}$ to 3×10^{-3}, respectively. Within this time frame HNO_3 would be expected to be severely depleted in the kinetic limit. Gas diffusion limitations will increase these time scales. For example, as graphed by Seinfeld and Pandis on page 632, the mass transfer time for a 30 μm diameter particle, assuming $\gamma = 0.005$, is approximately two times longer than the time in the kinetic limit.[30]

Assuming equilibrium HNO_3 coverages are attained in the atmosphere, the data collected here, modeled by the FHH multilayer model, can be used to estimate coverages of HNO_3 on cirrus clouds. Below, we apply this model to the data of NO_y observations in a lee-wave cloud from Weinheimer et al. and NO_y observations on cirrus from Meilinger et al.[12,13] The data in Table 1 describes the conditions of temperature, pressure, estimated gaseous HNO_3, condensed NO_y and cloud surface area reported in the studies of Weinheimer et al. and Meilinger et al. The condensed phase NO_y is converted to a number of molecules cm^{-3} using the ideal gas law at the pressure and temperature provided in Table 1. This value is then divided by the surface area density of the cloud, also provided in Table 1, to yield a condensed phase range of coverages as the final column in Table 1. The ranges of coverages for the two data sets are shown as vertical solid lines in Figure 9. Also shown in Figure 9 is the FHH model assuming several pressures of HNO_3. The pressures used for the FHH model, shown as dashed curved lines outlining the shaded area in Figure 9, bracket the pressure range to include both the Weinheimer et al. and Meilinger et al. pressures, $P_{HNO_3} = 3.5 \times 10^{-9} - 1.7 \times 10^{-8}$ Torr. The Weinheimer et al. measurements fall above and through the outlined region of possible gas-phase HNO_3 pressures, whereas the Meilinger et al. data fall below. Assuming surface uptake, the field observations should always lie at or below the FHH model. The model comes from experiments that have equilibrium coverages of HNO_3 on ice. Coverages in the atmosphere are not likely to be at equilibrium due to a number of reasons including the time to reach equilibrium and gas-phase diffusion limitations.

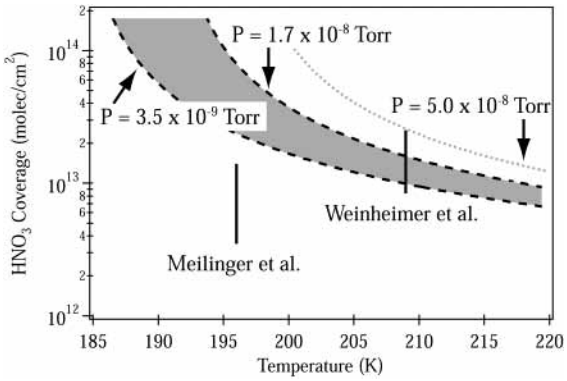

Figure 9. Semilog plot of HNO_3 coverage as a function of ice film temperature with modeled data from the FHH model at $P = 3.5 \times 10^{-9}$ and 1.7×10^{-8} Torr. The two solid lines indicate the range in coverage outlined by Weinheimer et al. ($T = 209$ K) and Meilinger et al. ($T = 196$ K). The measured data should fall at or below the model for surface uptake.

The Weinheimer et al. data is difficult to directly compare because they had no direct measurements of gas-phase HNO_3, only of gas-phase NO_y. On the basis of previous lab results from Zondlo et al. and Abbatt, Weinheimer et al. infer complete loss of gas-phase HNO_3 to the wave cloud yielding the ratio of gas-phase HNO_3/NO_y as 10−20% (25−75 pptv). In order for the Weinheimer et al. data to fall below the model, the HNO_3 pressure would need to be $P_{HNO_3} = 5.0 \times 10^{-8}$ Torr consistent with a HNO_3/NO_y ratio of 50% (375 pptv). A value of 50%

HNO_3/NO_y ratio is quite reasonable as explained in Weinheimer et al. Another possible explanation again refers to the solubility of HNO_3 in the ice particles. A particle with a 10 μm radius at $T = 209$ K and $P_{HNO_3} = 5 \times 10^{-8}$ Torr could contain an HNO_3 mole fraction of 2.9×10^{-7} yielding an apparent HNO_3 surface coverage of 9.06×10^{12} molecules cm^{-2}. This value is at the lower end of the observed uptakes by Weinheimer et al.

The Meilinger et al. data falls slightly below the model given the range of pressures. However, the model is being used outside of the measurement range and thus larger errors are expected. Thus, the overall agreement between the model and data is quite good. One possible reason for the slightly lower observations than modeled would be that the particles had not yet equilibrated with the gaseous HNO_3 due to gas-phase diffusion and uptake limitations. However, Meilinger et al. show that their particles were exposed to gas-phase HNO_3 for approximately 20 h, which may have been sufficient for equilibration depending on the uptake efficiency values at $T = 196$ K. Meilinger et al. propose that HNO_3 was mainly contained in supercooled ternary solutions (STS) coexisting with almost HNO_3-free ice.[13] Laboratory experiments which include the presence of H_2SO_4 and future field observations of gaseous and condensed HNO_3 in cirrus clouds under a variety of conditions would be very useful in constraining the models further.

Acknowledgment. M.A.T. would like to thank NASA-SASS and NSF-ATM for funding. J.E.S. acknowledges support from NASA (ESS-01-0000-0052). We also thank the reviewers for their insightful comments and Michel Rossi and Jon Abbatt for helpful information about their experiments.

References and Notes

(1) Chatfield, R. B. *Geophys. Res. Lett.* **1994**, *21*, 2705−2708.

(2) Hauglustaine, D. A.; Ridley, B. A.; Solomon, S.; Hess, P. G.; Madronich, S. *Geophys. Res. Lett.* **1996**, *23*, 2609−2612.

(3) Lary, D. J.; Lee, A. M.; Toumi, R.; Newchurch, M. J.; Pirre, M.; Renard, J. B. *J. Geophys. Res.* **1997**, *102*, 3671−3682.

(4) Goodman, A. L.; Bernard, E. T.; Grassian, V. H. *J. Phys. Chem. A* **2001**, *105*, 6443−6457.

(5) Tabazadeh, A.; Jacobson, M. Z.; Singh, H. B.; Toon, O. B.; Lin, J. S.; Chatfield, R. B.; Thakur, A. N.; Talbot, R. W.; Dibb, J. E. *Geophys. Res. Lett.* **1998**, *25*, 4185−4188.

(6) Underwood, G. M.; Li, P.; Al-Abadleh, H.; Grassian, V. H. *J. Phys. Chem. A* **2001**, *105*, 6609−6620.

(7) Lawrence, M. G.; Crutzen, P. J. *Tellus B* **1998**, *50*, 263−289.

(8) Tabazadeh, A.; Toon, O. B.; Jensen, E. J. *Geophys. Res. Lett.* **1999**, *26*, 2211−2214.

(9) Zondlo, M. A.; Barone, S. B.; Tolbert, M. A. *Geophys. Res. Lett.* **1997**, *24*, 1391−1394.

(10) Abbatt, J. P. D. *Geophys. Res. Lett.* **1997**, *24*, 1479−1482.

(11) Arora, O. P.; Cziczo, D. J.; Morgan, A. M.; Abbatt, J. P. D.; Niedziela, R. F. *Geophys. Res. Lett.* **1999**, *26*, 3621−3624.

(12) Weinheimer, A. J.; Campos, T. L.; Walega, J. G.; Grahek, F. E.; Ridley, B. A.; Baumgardner, D.; Twohy, C. H.; Gandrud, B.; Jensen, E. J. *Geophys. Res. Lett.* **1998**, *25*, 1725−1728.

(13) Meilinger, S. K.; Tsias, A.; Dreiling, V.; Kuhn, M.; Feigl, C.; Ziereis, H.; Schlager, H.; Curtius, J.; Sierau, B.; Arnold, F.; Zoger, M.; Schiller, C.; Peter, T. *Geophys. Res. Lett.* **1999**, *26*, 2207−2210.

(14) Hudson, P. K.; Zondlo, M. A.; Tolbert, M. A. *J. Phys. Chem. A* **2002**, *106*, 2282−2888.

(15) Golden, D. M.; Spokes, G. N.; Benson, S. W. *Angew. Chem., Internat. Edit.* **1973**, *12*, 534−546.

(16) Greenler, R. G. *J. Chem. Phys.* **1966**, *44*, 310−315.

(17) Marti, J.; Mauersberger, K. *Geophys. Res. Lett.* **1993**, *20*, 363−36.

(18) Aguzzi, A.; Rossi, M. J. *Phys. Chem. Chem. Phys.* **2001**, *3*, 3707−3716.

(19) *CRC Handbook of Chemistry and Physics*; 73rd ed.; Lide, D. R., Ed.; CRC Press: Boca Raton, 1992−1993.

(20) Hanson, D. R. *Geophys. Res. Lett.* **1990**, *17*, 421−423.

(21) Hanson, D.; Mauersberger, K. *Geophys. Res. Lett.* **1988**, *15*, 855−858.

(22) Zondlo, M. A.; Barone, S. B.; Tolbert, M. A. *J. Phys. Chem. A* **1998**, *102*, 5735−5748.

(23) Toon, O. B.; Tolbert, M. A.; Koehler, B. G.; Middlebrook, A. M.; Jordan, J. *J. Geophys. Res.* **1994**, *99*, 25631−25654.

(24) http://www.rsc.org/suppdata/CP/B1005460/tables.pdf.

(25) Hanson, D. R. *Geophys. Res. Lett.* **1992**, *19*, 2063−2066.

(26) Boudart, M.; Djéga-Mariadassou, G. *Kinetics of Heterogeneous Catalytic Reactions*; Princeton University Press: Princeton, New Jersey, 1984.

(27) Jayne, J. T.; Duan, S. X.; Davidovits, P.; Worsnop, D. R.; Zahniser, M. S.; Kolb, C. E. *J. Phys. Chem.* **1991**, *95*, 6329−6336.

(28) JaeckerVoirol, A.; Ponche, J.; Mirabel, P. *J. Geophys. Res.* **1990**, *1995*, 11 857−11 863.

(29) Thibert, E.; Domine, F. *J. Phys. Chem. B* **1998**, *102*, 4432−4439.

(30) Seinfeld, J. H.; Pandis, S. N. *Atmospheric Chemistry and Physics: From air pollution to climate change*; John Wiley & Sons: New York, 1997.

(31) Jensen, E. J.; Toon, O. B.; Tabazadeh, A.; Sachse, G. W.; Anderson, B. E.; Chan, K. R.; Twohy, C. W.; Gandrud, B.; Aulenback, S. M.; Heymsfield, A.; Hallett, J.; Gary, B. *Geophys. Res. Lett.* **1998**, *25*, 1363−1366.

(32) Baumgardner, D.; Gandrud, B. E. *Geophys. Res. Lett.* **1998**, *25*, 1129−1132.

(33) Schiller, C.; Afchine, A.; Eicke, N.; Feigl, C.; Fischer, H.; Giez, A.; Konopka, P.; Schlager, H.; Tuitjer, F.; Wienhold, F. G.; Zoger, M. *Geophys. Res. Lett.* **1999**, *26*, 2219−2222.

(34) Feigl, C.; Schlager, H.; Ziereis, H.; Curtius, J.; Arnold, F.; Schiller, C. *Geophys. Res. Lett.* **1999**, *26*, 2215−2218.